PHYSICAL REVIEW D **83,** 023517 (2011)

Kinetic analysis of thermally relativistic flow with dissipation

Ryosuke Yano* and Kojiro Suzuki†
Department of Advanced Energy, University of Tokyo, 5-1-5 Kashiwanoha, Kashiwa, Chiba 277-8561, Japan

(Received 5 October 2010; published 20 January 2011)

Nonequilibrium flow of thermally relativistic matter with dissipation is considered in the framework of the relativistic kinetic theory. As an object of the analysis, the supersonic rarefied flow of thermally relativistic matter around the triangle prism is analyzed using the Anderson-Witting model. Obtained numerical results indicate that the flow field changes in accordance with the flow velocity and temperature of the uniform flow owing to both effects derived from the Lorentz contraction and thermally relativistic effects, even when the Mach number of the uniform flow is fixed. The profiles of the heat flux along the stagnation streamline can be approximated on the basis of the relativistic Navier-Stokes-Fourier (NSF) law except for a strong nonequilibrium regime such as the middle of the shock wave and the vicinity of the wall, whereas the profile of the heat flux behind the triangle prism cannot be approximated on the basis of the relativistic NSF law owing to rarefied effects via the expansion behind the triangle prism. Additionally, the heat flux via the gradient of the static pressure is non-negligible owing to thermally relativistic effects. The profile of the dynamic pressure is different from that approximated on the basis of the NSF law, which is obtained by the Eckart decomposition. Finally, variations of convections of the mass and momentum owing to the effects derived from the Lorentz contraction and thermally relativistic effects are numerically confirmed.

DOI: 10.1103/PhysRevD.83.023517 PACS numbers: 98.80.Jk, 47.75.+f

I. INTRODUCTION

Relativistic fluid dynamics have become a very significant issue in astrophysics [1] or high-energy physics [2] related to quark-gluon plasma. However, the conventional analysis of relativistic fluids is mostly limited to the analysis using the relativistic Euler equation [3], because the construction of the relativistic hydrodynamic equation with dissipation includes two serious problems. One is the problem of acausality [4]. The other is the problem of instability [4]. The acausality emerges in the diffusion term in the relativistic Navier-Stokes-Fourier (NSF) equation owing to its parabolic form. The improvements to the most classic theory of the relativistic NSF equation proposed by Eckart [5], which involves the above two problems, were carried out by many researchers. For example, another frame, which is different from that proposed by Eckart, was proposed by Landau-Lifshitz [6], or Tsumura-Kunihiro [7]. Another approach to avoid the problem of acausality was proposed by introducing the second-order hydrodynamics [8] and the hydrodynamics above the second order [9,10] or the telegraphist's equation [11]. In the recent studies [12,13], the acausality can be dismissed from the viewpoint of physical scaling regardless of the parabolic form. Meanwhile, the numerical solver of the relativistic hydrodynamics equation with dissipation is developed. For example, the numerical code to solve the Israel-Stewart equation was developed by Bouras *et al.* [14], and the reduced dissipative general relativistic hydrodynamics equation was solved for the black hole formation by Duez *et al.* [15].

The relativistic Boltzmann equation is known to be free from the above mentioned problems [16], namely, acausality and instability. However, direct simulation of the relativistic Boltzmann equation has not been reported owing to a more complex collision term than that of the nonrelativistic Boltzmann equation, whereas the analysis using stochastic method has been reported [17,18]. Fortunately, we have the Bhatnagar-Gross-Krook (BGK) [19] type kinetic equations as a reduced model of the relativistic Boltzmann equation. The most classic relativistic BGK-type model is the Marle model [20]. Afterwards, the Anderson-Witting (AW) model [21] was proposed as an extended model of the Marle model. In this paper, we discuss the relativistic flow with dissipation by solving the AW model instead of solving the relativistic hydrodynamic equation or the relativistic Boltzmann equation, whereas Mendoza *et al.* [22] discussed the relativistic flow with dissipation by applying the Marle model to the Lattice-Boltzmann method. The equilibrium function is the Maxwell-Jättner function by following a recent study [23], although there exists a proposal of another form [24] of the equilibrium function. As a decomposition method, the Eckart decomposition is used, because significant quantities in the calculation of the AW model, namely, conserved quantities (i.e., the density, momentum, and energy), can be correctly decomposed by the Eckart decomposition.

As an object of analysis, the supersonic rarefied flow of thermally relativistic matter around the triangle prism, which has an infinite length in the direction perpendicular to the uniform flow, is considered in flat spacetime,

---

*yano@daedalus.k.u-tokyo.ac.jp
†kjsuzuki@k.u-tokyo.ac.jp

1550-7998/2011/83(2)/023517(12)

whereas the extension to the curved spacetime is studied by Yano *et al.* [25]. Thermally relativistic matter is characterized under the condition $\zeta = mc^2/(k\theta) \leq 100$ (m: mass, c: speed of light, k: Boltzmann constant, θ: temperature). In particular, transport coefficients markedly change at $\zeta \leq 10$ [26]. Such relativistic changes in thermodynamics from the nonrelativistic thermodynamics (i.e., change in definition of the specific heat, transport coefficients as the functions of the temperature (or ζ), which are different from those in the nonrelativistic case) are called thermally relativistic effects.

The flow field around the triangle prism includes some interesting phenomena, such as the shock wave, expansion wave and vortex. The nonrelativistic flow field is determined from the Mach number (M_∞, where the subscript ∞ indicates the state in the uniform flow) and the rarefaction parameter such as Knudsen number [27] of the uniform flow, whereas the relativistic flow field is determined from ζ_∞ and the Lorentz factor (γ_∞) of the uniform flow together with M_∞ and the rarefaction parameter. Such effects owing to the Lorentz contraction and thermally relativistic effects are explicitly expressed in the relativistic NSF equation in Sec. III to help later discussions on relativistic effects on the convection of fluids in Sec. IV. In this paper, ζ is changed for the parametric study using the fixed M_∞ and the rarefaction parameter $4\pi\sigma n_\infty L$ (σ: collision cross section, n_∞: number density of the uniform flow, L: representative length), where γ_∞ is readily determined using ζ_∞ and M_∞. On the basis of the fact that the BGK model is the nonrelativistic limit ($\zeta \to \infty \wedge \gamma = 1$) of the AW model, we discuss relativistic effects via ζ and γ for the fixed $M_\infty = 3.247$ through comparisons among flow fields obtained with the AW model using three types of ζ_∞, namely, $\zeta_\infty = 45$, 60 and 75, and the BGK model. In our calculation, the uniform flow is sufficiently rarefied to observe the shock wave structure. Consequently, rarefied effects, which are described using terms over the Burnett order [28], are significant in the nonequilibrium regime of the flow field. The AW model presumably yields a solution similar to that obtained using the relativistic Boltzmann equation in such a rarefied regime, as the BGK equation yields a solution similar to that obtained using the nonrelativistic Boltzmann equation in the rarefied regime [27]. Profiles of the heat flux along the stagnation streamline (SSL) can be approximated using the relativistic NSF law but for the strong nonequilibrium regime such as the middle of the shock wave and the vicinity of the wall. On the other hand, profiles of the heat flux along the wake streamline (WSL) cannot be approximated using the relativistic NSF law owing to the rarefied effects via the expansion behind the triangle prism. Additionally, the heat flux via the gradient of the static pressure is nonnegligible owing to thermally relativistic effects. Profiles of the dynamic pressure indicate that the magnitude of the obtained dynamic pressure is one digit smaller than that approximated by the relativistic NSF law, and the sign of the obtained dynamic pressure is opposite to that approximated by the relativistic NSF law.

This paper is organized as follows. In Sec. II, we review the numerical method by Yano *et al.* [29] to solve the AW model. In Sec. III, the effects derived from the Lorentz contraction and thermally relativistic effects are explicitly expressed in the relativistic NSF equation. In Sec. IV, the supersonic rarefied flow of thermally relativistic matter around the triangle prism is numerically analyzed. In Sec. V, we provide concluding remarks.

II. NUMERICAL METHOD OF SOLVING THE ANDERSON-WITTING MODEL

The Anderson-Witting model is given by [21]

$$p^\alpha \frac{\partial f}{\partial x^\alpha} = \frac{U_L^\alpha p_\alpha}{c^2\tau}(f^{(0)} - f), \tag{1}$$

where $x^\alpha = (ct, x^1, x^2, x^3)$, $p^\alpha = m\gamma(v)(c, v^1, v^2, v^3)$, in which m is the particle mass and $\gamma(v)$ is the Lorentz factor given by $\gamma(v) = 1/\sqrt{1 - v^2/c^2}$, c is the speed of light and v^i is the ith component of the particle velocity for $i(= 1, 2, 3)$, and $f \equiv f(x^\alpha, p^i)$ $(i = 1, 2, 3)$ is the distribution function. $f^{(0)}$ in Eq. (1) is an equilibrium function called the Maxwell-Jüttner function, and can be defined as

$$f^{(0)}(n, \theta, u) = \frac{n}{4\pi m^2 ck\theta K_2(\zeta)} e^{-(U^\alpha p_\alpha)/(k\theta)}, \tag{2}$$

where ζ is given by $\zeta = \frac{mc^2}{k\theta}$, in which k is the Boltzmann constant, and θ is the temperature. K_n is the nth order modified Bessel function of the second kind and U_L^α is the four velocity of flow defined by Landau-Lifshitz [6] and written as

$$U_L^\alpha = U^\alpha + \frac{q^\alpha}{ne + p}, \tag{3}$$

where $U^\alpha = \gamma(u)(c, u^i)$, in which u^i $(i = 1, 2, 3)$ is the i-th component of the flow velocity, is the four velocity of the flow, and q^α is the four heat flux, which is defined in Eq. (13). τ in Eq. (1) is defined for the hard sphere molecule as [26]

$$\tau = \frac{1}{4n\pi\sigma v_s}, \tag{4}$$

$$v_s = \sqrt{\frac{\zeta^2 + 5G\zeta - G^2\zeta^2}{G(\zeta^2 + 5G\zeta - G^2\zeta^2 - 1)}\frac{k\theta}{m}}, \tag{5}$$

where v_s is the relativistic speed of sound and $G = K_3(\zeta)/K_2(\zeta)$. In this paper, we exclude massless particles. Then the Anderson-Witting model defined in Eq. (1) can be rewritten as

$$\frac{\partial f}{\partial t} + v^i \frac{\partial f}{\partial x^i} = \left(\gamma(u)(c, u_i) + \frac{q^\alpha}{ne + p}\right)(c, -v^i)^T \frac{(f^{(0)} - f)}{c^2 \tau}. \tag{6}$$

In the nonrelativistic limit, namely, $\gamma(u) = 1 \wedge \zeta = \infty$, Eq. (6) approximates to the BGK model. In general, the distribution function is $f = f(t, x^1, x^2, x^3, v^1, v^2, v^3)$, which has a one-to-one correspondence to $f = f(t, x^1, x^2, x^3, p^1, p^2, p^3)$. In this work, we use $f = f(t, x^1, x^2, x^3, v^1, v^2, v^3)$ instead of $f = f(t, x^1, x^2, x^3, p^1, p^2, p^3)$. To calculate the projected moments, we transform $d^3\mathbf{p}/p^0$ into velocity space $d^3\mathbf{v}$ as

$$\frac{d^3\mathbf{p}}{p^0} = J \left| \frac{\partial p^i}{\partial v^j} \right| \Big/ (m\gamma(v)c) = \frac{m^2 \gamma(v)^4}{c} d^3\mathbf{v}. \tag{7}$$

From Eq. (7), the particle four-flow N^α can be written as

$$N^\alpha = c \int_{\mathcal{R}^3} p^\alpha f d^3\mathbf{p}/p^0 = \int_{\mathcal{V}^3} m^3 \gamma(v)^5 (c, v^i) f d^3\mathbf{v}. \tag{8}$$

The momentum-energy tensor $T^{\alpha\beta}$ can also be written as

$$\begin{aligned} T^{\alpha\beta} &= c \int_{\mathcal{R}^3} p^\alpha p^\beta f \frac{d^3\mathbf{p}}{p^0} \\ &= \int_{\mathcal{V}^3} m^4 \gamma(v)^6 (c, v^i)(c, v^j) f d^3\mathbf{v}. \end{aligned} \tag{9}$$

In Eqs. (8) and (9), $\mathcal{V}^3$ is velocity space stretched by $\{\mathcal{V}^3; |v| \le c\}$, where $|v| = \sqrt{(v^1)^2 + (v^2)^2 + (v^3)^2}$. Projected moments, the number density n, pressure deviator $p^{\langle\alpha\beta\rangle}$, static pressure p, dynamic pressure ϖ, heat flux q^α and energy per particle e are obtained as [5]

$$n = \frac{1}{c^2} N^\alpha U_\alpha, \tag{10}$$

$$p^{\langle\alpha\beta\rangle} = (\Delta^\alpha_\gamma \Delta^\beta_\delta - \tfrac{1}{3}\Delta^{\alpha\beta}\Delta_{\gamma\delta}) T^{\delta\gamma}, \tag{11}$$

$$p + \varpi = -\tfrac{1}{3}\Delta_{\alpha\beta} T^{\alpha\beta}, \tag{12}$$

$$q^\alpha = \Delta^\alpha_\gamma U_\beta T^{\beta\gamma}, \tag{13}$$

$$e = \frac{1}{nc^2} U_\alpha T^{\alpha\beta} U_\beta, \tag{14}$$

where the projector $\Delta^{\alpha\beta}$ is

$$\Delta^{\alpha\beta} = \eta^{\alpha\beta} - \frac{1}{c^2} U^\alpha U^\beta, \tag{15}$$

where $\eta^{\alpha\beta}$ is the Minkowski metric. In our numerical code, the second-order total variable diminishing scheme [30] is used for the left-hand side of Eq. (6), and second-order Runge-Kutta time integration is used for the time integration of Eq. (6).

For convenience, nondimensionalization is carried out as

$$\begin{aligned} &\tilde{n} = \frac{n}{n_\infty}, \quad \tilde{v}^i = \frac{v_i}{c}, \quad \tilde{u}^i = \frac{u^i}{c} \quad \tilde{e} = \frac{e}{mc^2}, \quad \tilde{q}^\alpha = \frac{q^\alpha}{n_\infty m c^3}, \\ &\tilde{x}^i = \frac{x^i}{L}, \quad \tilde{t} = \frac{t}{t_\infty}, \quad t_\infty = \frac{L}{c}, \end{aligned} \tag{16}$$

where L is the representative length in the observer's frame.

With these nondimensionalized quantities defined in Eq. (16), the Maxwell-Jüttner function in Eq. (2) can be nondimensionalized as

$$\tilde{f}^{(0)} = \frac{(mc)^3}{n_\infty} f^{(0)} = \frac{\tilde{n}\zeta}{4\pi K_2(\zeta)} e^{-\zeta\gamma(\tilde{u})\gamma(\tilde{v})(1 - \tilde{u}^i \tilde{v}^i)}. \tag{17}$$

The left-hand side of Eq. (6) represents the propagation of molecules with velocity vector (v^1, v^2, v^3) in physical space (x^1, x^2, x^3). This formulation for molecular propagation in physical space does not involve relativistic effects. As a result, in body-fitted curvilinear coordinates (ξ^1, ξ^2, ξ^3), molecules with a velocity vector (v^1, v^2, v^3) in (x^1, x^2, x^3) propagate with velocity $(v^1_\xi, v^2_\xi, v^3_\xi)$. Equation (6) can therefore be written in a body-fitted curvilinear coordinate (ξ^1, ξ^2, ξ^3) as

$$\begin{aligned} &\frac{\partial \tilde{f}}{\partial t} + \frac{\partial v^i_\xi \tilde{f}}{\partial \xi^i} = \left(\gamma(u)(c, u_i) + \frac{q^\alpha}{ne + p}\right)(c, -v^i)^T \times \frac{(\tilde{f}^{(0)} - \tilde{f})}{c^2 \tau}, \\ &\qquad \tilde{f} = f/\tilde{J}, \end{aligned} \tag{18}$$

where $\tilde{J}$ is the Jacobian between x^i and ξ^i.

The wall condition must also be considered. In this paper, complete diffusion at the wall [26] is assumed. From conservation of the mass flux to the wall and by setting the ξ^2 axis as the normal vector to the plane element of the wall, we obtain

$$f_w = f(v^2_\xi < 0), \tag{19}$$

$$f_w/n_w = f^{(0)}(1, \theta_w, 0)(v^2_\xi \ge 0), \tag{20}$$

$$n_w = \frac{-\int_{v^2_\xi < 0} v^2_\xi f \gamma^5 d^3\mathbf{v}}{\int_{v^2_\xi \ge 0} v^2_\xi f_w/n_w \gamma^5 d^3\mathbf{v}}, \tag{21}$$

where f_w is the distribution function on the wall. n_w is the number density reflected from the wall and θ_w is the temperature of the wall.

III. RELATIVISTIC NSF LAW AND NSF EQUATION

In this section, we review the relativistic NSF law to discuss the obtained numerical results in the framework of the relativistic NSF law obtained by the first-order approximation of the Chapman-Enskog expansion on the basis of the Eckart decomposition. Next, we explicitly express the forgoing two types of relativistic effects in the relativistic NSF equation.

A. Relativistic NSF law by the first-order approximation of the Chapman-Enskog expansion

The relativistic NSF law obtained by the first-order approximation of the Chapman-Enskog expansion is written in a flat spacetime as [26,31]

$$\varpi_{\rm NSF} = -\eta\nabla_\alpha U^\alpha, \tag{22}$$

$$p_{\rm NSF}^{\langle\alpha\beta\rangle} = 2\mu[\tfrac{1}{2}(\Delta^\alpha_\gamma\Delta^\beta_\delta + \Delta^\alpha_\delta\Delta^\beta_\gamma) - \tfrac{1}{3}\Delta^{\alpha\beta}\Delta_{\gamma\delta}]\nabla^\gamma U^\delta, \tag{23}$$

$$q^\alpha_{\rm NSF} = \lambda\left(\nabla^\alpha\theta - \frac{\theta}{nh_E}\nabla^\alpha p\right), \tag{24}$$

where η is the bulk viscosity, μ is the viscosity coefficient, λ is the thermal conductivity, $h_E = ne + p$ and ∇^α is defined as

$$\nabla^\alpha = \left(\eta^{\alpha\beta} - \frac{1}{c^2}U^\alpha U^\beta\right)\partial_\beta = \Delta^{\alpha\beta}\partial_\beta. \tag{25}$$

Figure 1 shows transport coefficients (η, λ, μ) [26] versus ζ for a hard sphere particle obtained using the AW model and the relativistic Boltzmann equation in the range of $7 \leq \zeta \leq 75$, which corresponds to the calculated dynamic range of ζ discussed in Sec. IV. All the transport coefficients are calculated using the first-order approximation of the Chapman-Enskog expansion [26]. In this regime of ζ, $\eta_{\rm AW} < \eta_B$, $\lambda_{\rm AW} < \lambda_B$ and $\mu_B < \mu_{\rm AW}$. In the thermally relativistic limit $\zeta \to 0$, the viscosity coefficient approximates to infinity, the thermal conductivity approximates to the constant value, and the bulk viscosity approximates to zero [26].

$q^\alpha_{\rm NSF}$ in Eq. (24) indicates that the heat flux depends on not only the gradient of the temperature but also the gradient of the static pressure. Then, we define the heat flux via the gradient of the pressure as $(q^\alpha_t)_{\rm NSF}$ and the heat flux via the gradient of the pressure $(q^\alpha_p)_{\rm NSF}$ as

$$(q^\alpha_t)_{\rm NSF} = \lambda\nabla^\alpha\theta, \tag{26}$$

$$(q^\alpha_p)_{\rm NSF} = -\lambda\frac{\theta}{nh_E}\nabla^\alpha p, \tag{27}$$

where $\frac{\theta}{nh_E}$ approximates to zero by $\zeta \to \infty$. As a result, $(q^\alpha_p)_{\rm NSF}$ vanishes in the thermally nonrelativistic limit ($\zeta \to \infty$). In Sec. IV, $(q^\alpha_p)_{\rm NSF}$ is numerically compared with $(q^\alpha_t)_{\rm NSF}$.

B. Explicit expression of relativistic effects in the relativistic NSF equation

The normal form of the relativistic NSF equation is written in flat spacetime (t, x^i) $(i = 1, 2, 3)$ as [32]

$$\frac{\partial\gamma(u)\rho}{\partial t} + \frac{\partial}{\partial x^i}(\gamma(u)\rho u^i) = 0, \tag{28}$$

$$\frac{\partial G(\gamma(u))^2\rho u^i}{\partial t} + \frac{\partial}{\partial x^j}\{G(\gamma(u))^2\rho u^i u^j\} + \frac{\partial p}{\partial x^i} + \Pi^i = 0, \tag{29}$$

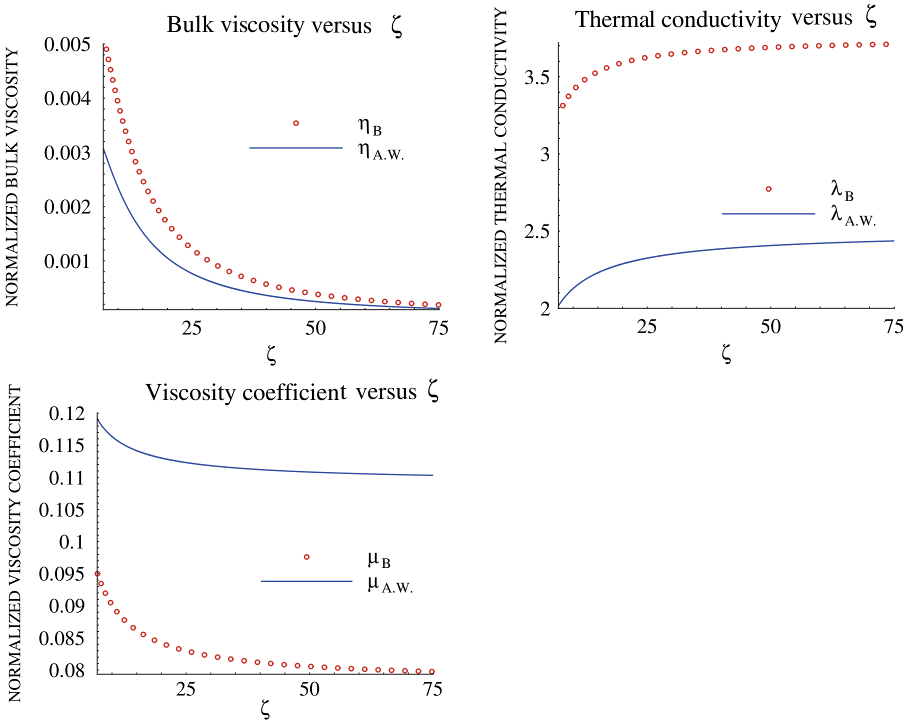

FIG. 1 (color online). Transport coefficients versus ζ in calculated range $7 \leq \zeta \leq 75$, (subscripts B, relativistic Boltzmann equation, Anderson-Witting model).

$$\frac{\partial\gamma(u)E}{\partial t}+\frac{\partial}{\partial x^i}(\gamma(u)Eu^i)+p\left(\frac{\partial\gamma(u)}{\partial t}+\frac{\partial(\gamma(u)u^i)}{\partial x^i}\right)+\Lambda=0, \tag{30}$$

where $\rho(=nm)$ is the density, u^i is the velocity of the flow, p is the static pressure, $E=ne$ is the internal energy, $\gamma(u)=1/\sqrt{1-u^2/c^2}$ is the Lorentz factor, Π^i is the momentum dissipation term and Λ is the energy dissipation term. Dissipative terms Π^i and Λ using ϖ, $p^{\langle\alpha\beta\rangle}$ and q^α are defined in [32].

At first, Eqs. (28)–(30) can be rewritten for nonzero mass particles as

$$\underbrace{\frac{\partial\rho}{\partial t}+\frac{\partial}{\partial x^i}(\rho u^i)}_{\text{NRNSF}}+\rho\underbrace{\mathcal{S}}_{\substack{0\\ L}}=0, \tag{31}$$

$$\underbrace{\frac{\partial(\rho u^i)}{\partial t}+\frac{\partial}{\partial x^j}(\rho u^i u^j+p)+\Pi^i_{\rm NR}}_{\text{NRNSF}}+\rho u^i\underbrace{\mathcal{S}}_{\substack{1\\ L+T}}+\underbrace{\frac{1}{G(\gamma(u))^2}}_{L+T}\Pi^i-\Pi^i_{\rm NR}+\left(\underbrace{\frac{1}{G(\gamma(u))^2}}_{L+T}-1\right)\frac{\partial p}{\partial x^i}=0 \tag{32}$$

$$\underbrace{\frac{\partial E_{\rm NR}}{\partial t}+\frac{\partial}{\partial x^i}(E_{\rm NR}u^i)+p\frac{\partial u^i}{\partial x^i}+\Lambda_{\rm NR}}_{\text{NRNSF}}+\underbrace{\frac{1}{\gamma(u)}}_{L+T}\Lambda-\Lambda_{\rm NR}+\frac{\partial}{\partial t}(\underbrace{\delta E}_{T})+\frac{\partial}{\partial x^i}(\underbrace{\delta E}_{T}u^i)+(\underbrace{E}_{T}+p)\underbrace{\mathcal{S}}_{\substack{0\\ L}}=0, \tag{33}$$

$$\text{where } \mathcal{S}_0=\left(\frac{\partial}{\partial t}+u^i\frac{\partial}{\partial x^i}\right)\ln\gamma(u),$$

$$\mathcal{S}_1=\left(\frac{\partial}{\partial t}+u^i\frac{\partial}{\partial x^i}\right)\ln(G(\gamma(u))^2),$$

$$\delta E=nmc^2\left(G-\frac{1}{\zeta}\right)-\left(\underbrace{\frac{3}{2}nk\theta}_{E_{\rm NR}}+nmc^2\right). \tag{34}$$

In Eqs. (31)–(33), the terms with subscript L have effects derived from the Lorentz contraction, the terms with subscript T have thermally relativistic effects and the terms with $L+T$ have both effects derived from the Lorentz contraction and thermally relativistic effects.

Dissipation terms Π^i and Λ change in accordance with ζ as shown in Fig. 1 in addition to $\gamma(u)$ as shown in Eqs. (22)–(24). From Eqs. (31)–(34), we find some modifications to the nonrelativistic NSF (NRNSF) equation. For $1\ll\ln\gamma(u)$, the convections via $\rho\mathcal{S}_0$, $\rho u^i\mathcal{S}_1$ and $(E+p)\mathcal{S}_0$ can be more dominant than the convections indicated by the NRNSF equation in Eqs. (31)–(33). For $\gamma(u)\simeq 1$, thermally relativistic effects become significant, in terms with $\mathcal{S}_1$ and δE. In particular, for $1\ll G$ ($\zeta\ll 1$), namely, the thermally relativistic limit, the convection of momentum attributable to the term $\rho u^i\mathcal{S}_1$ can be dominant in Eq. (32), δE approximates to $\frac{3}{2}nk\theta$ in Eq. (33), and dissipative terms approximate to $\lim_{\zeta\to 0}\frac{\Pi^i}{G(\gamma(u))^2}\sim O(\zeta^0)$ and $\lim_{\zeta\to 0}\Lambda\sim O(\zeta)$ [33]. Actually, effects by terms $\mathcal{S}_0$ and $\mathcal{S}_1$ in Eq. (34) are discussed through numerical analysis in Sec. IV.

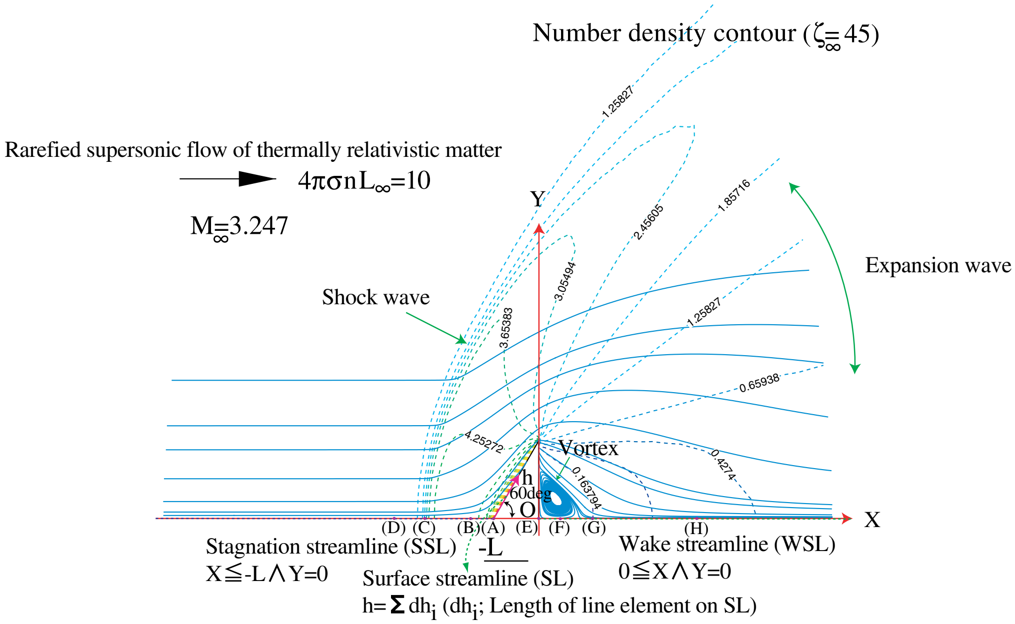

FIG. 2 (color online). Schematic of flow field.

IV. NUMERICAL ANALYSIS OF RAREFIED SUPERSONIC FLOW OF THERMALLY RELATIVISTIC MATTER AROUND TRIANGLE PRISM

The rarefied supersonic flow of thermally relativistic matter around the triangle prism is numerically analyzed using the AW and BGK models. Particles are assumed to be hard sphere particles with common mass m and diameter d. For easier comprehension of physical conditions, for the observer's frame the absolute standard of rest is used as the hypothetical inertial frame. We use (X, Y, Z) instead of (x^1, x^2, x^3) and (v^x, v^y, v^z) instead of (v^1, v^2, v^3) and consider only XY plane, because the triangle prism has an infinite length in the Z direction. The Mach number of the uniform flow, M_∞ is fixed to 3.247. Here, three types of ζ_∞, namely, $\zeta_\infty = 45$, 60 and 75 are used. As a result of $M_\infty = 3.247$, the velocity of the uniform flow is $u^x_\infty/c = 0.6$ for $\zeta_\infty = 45$, $u^x_\infty/c = 0.526$ for $\zeta_\infty = 60$ and $u^x_\infty/c = 0.472$ for $\zeta_\infty = 75$ from the definition of the speed of sound in Eq. (5). The rarefaction parameter of the uniform flow $4\pi\sigma n_\infty L$, which defines $1/(v_s\tau)$ in Eq. (4), is set to 10, where L is the representative length in the flow field. In the AW model, the relaxation rate τ depends on the four velocity of flow, four velocity of particles, temperature, number density, and heat flux q^α in Eq. (18), whereas the relaxation rate in the BGK model depends on the number density and the temperature. For the numerical grid, $(v^x, v^y, v^z, X, Y) = (64, 64, 64, 125, 60)$ is used. Numerical tests indicate that this numerical grid provides accurate simulations.

Figure 2 shows the schematic view of the flow field. The flow field in the regime of $Y < 0$ is omitted, which is the same as in the flow field in the regime of $0 \leq Y$, owing to the symmetry of the flow field. The vertex angle of the triangle prism is 120 degrees and the length of the side on the X axis is set to L as shown in Fig. 2. The SSL is defined by the line on the X axis with the range of $X \leq -L \wedge Y = 0$, the WSL is defined by the line on the X axis with the range of $0 \leq X \wedge Y = 0$, and the surface streamline (SL) is defined by the line on the surface of the triangle prism on the XY plane, where h in Fig. 2 is the distance measured from $(X, Y) = (-L, 0)$ along the SL. Figure 2 shows that the flow field includes the shock wave, expansion wave, and vortex, and that the flow field behind the triangle prism becomes more rarefied than the uniform flow owing to the

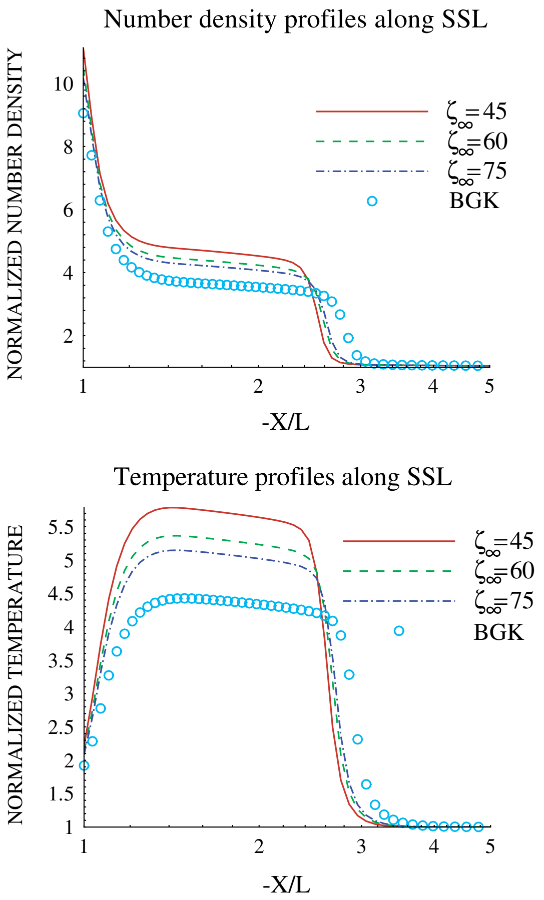

FIG. 3 (color online). Number density (top-left), Mach number (top-right), and temperature (bottom-left) profiles along the stagnation streamline.

strong expansion at $(X, Y) = (0, \sqrt{3}L/2)$, as shown in the contour of the number density in the case of $\zeta_\infty = 45$. The complete diffusion model on the wall is used as described in Sec. III. The temperature θ_w (ζ_w) of the wall is $3/2$ ($2/3$) times of θ_∞ (ζ_∞) in the uniform flow. Consequently, $\zeta_w = 30$ for $\zeta_\infty = 45$, $\zeta_w = 40$ for $\zeta_\infty = 60$ and $\zeta_w = 50$ for $\zeta_\infty = 75$.

Figure 3 shows the profiles of the number density, Mach number and temperature along the SSL. Profiles of the number density, Mach number and temperature obtained using the AW model are different from those obtained using the BGK model in each case of $\zeta_\infty = 45$, 60 and 75 owing to the relativistic Rankine-Hugoniot relation [34]. By increasing the temperature (flow velocity) of the uniform flow, the ratio of the number density (or temperature) behind the shock wave to that ahead of the shock wave becomes larger. Such a tendency is caused by the fact that the relativistic Rankine-Hugoniot relation depends on the Lorentz factor and temperature, whereas the nonrelativistic Rankine-Hugoniot relation depends on only the Mach number. The location of the shock wave obtained using the AW model with $\zeta_\infty = 75$ is similar to that obtained using the AW model with $\zeta_\infty = 60$, whereas the location of the shock wave obtained using the AW model with $\zeta_\infty = 45$ is different from that obtained using the AW model with $\zeta_\infty = 60$ and 75. Consequently, the increase (decrease) of ζ_∞ (θ_∞) moves the location of the shock toward the wall. As shown in Fig. 3, the profile of the Mach number obtained using the BGK model is similar to that obtained using the AW model with $\zeta_\infty = 45$, 60 and 75 behind the shock.

Figure 4 shows profiles of the number density, velocity, temperature and Mach number along the WSL. The increase in θ_∞ (u^x_∞) under a fixed Mach number ($M_\infty = 3.247$) yields the increase in the number density and temperature along the WSL. As shown in Fig. 4 (top-right), profiles of the flow velocity have the reverse flow regime due to the vortex. The bifurcation point, which determines the scale of the vortex, indicates that the vortex becomes larger with the increase in θ_∞ (u^x_∞). The profile of the Mach number obtained using the BGK model is similar to those obtained using the AW model.

Figure 5 shows profiles of the number density, slipped velocity [35], temperature and dynamic pressure along the SL. The increase in θ_∞ (u^x_∞) yields the increase in the number density, slipped velocity and temperature along the SL. Profiles of the number density obtained using the AW and BGK models have their peaks around $h/L \sim 0.2$, whereas all of number density profiles once drop behind the vertex ($h = 0$) and increase by $h/L \sim 0.2$. Profiles of

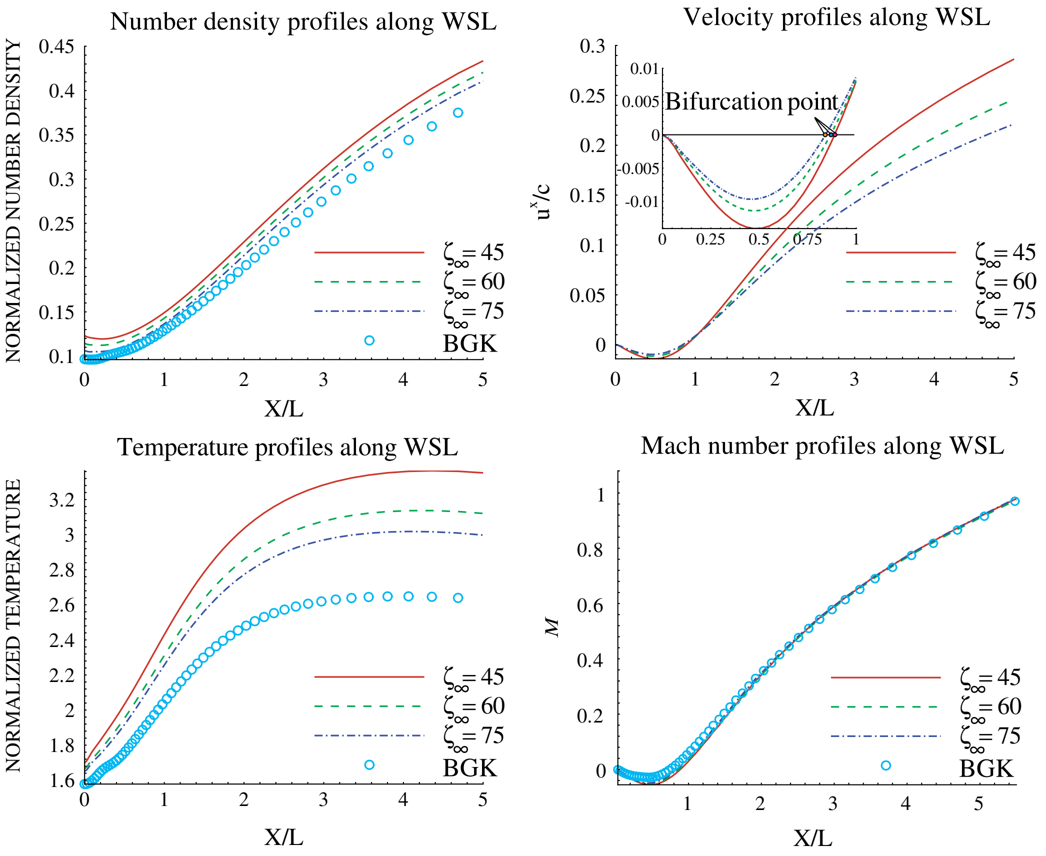

FIG. 4 (color online). Number density (top-left), velocity (top-right), temperature (bottom-left) and Mach number (bottom-right) profiles along the wake streamline.

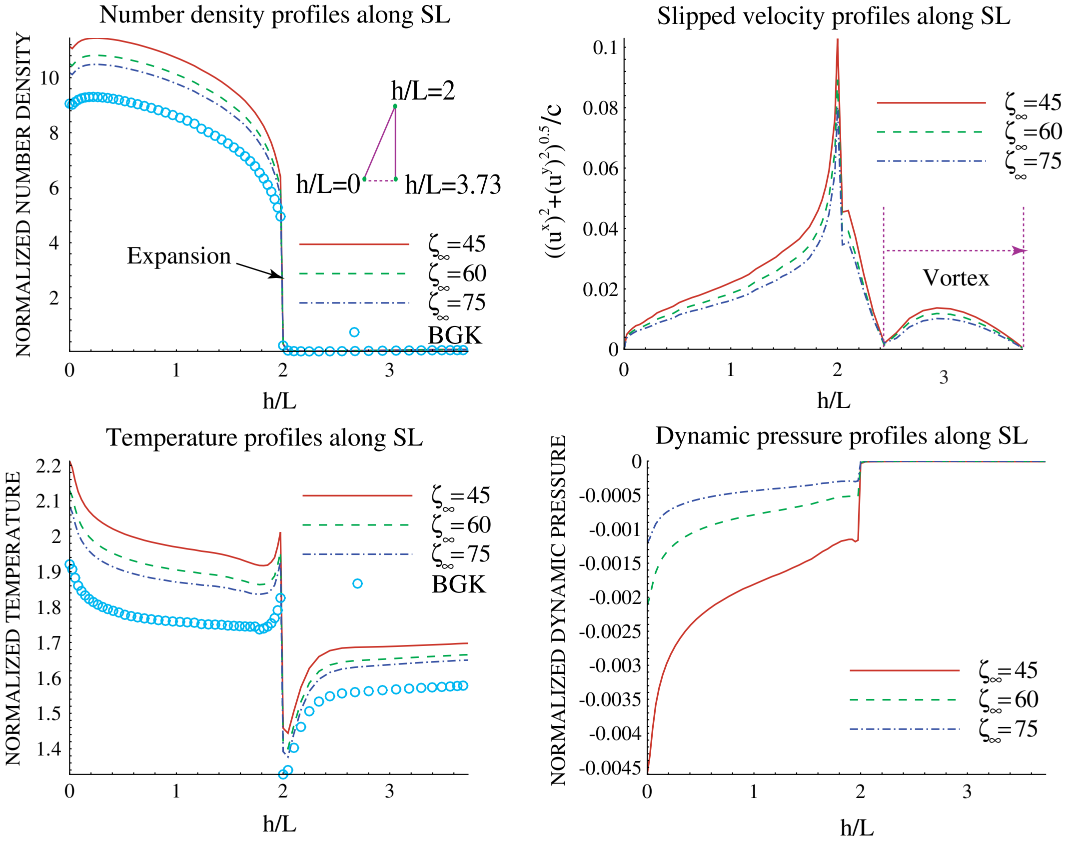
Number density profiles along SL
Slipped velocity profiles along SL
Temperature profiles along SL
Dynamic pressure profiles along SL

FIG. 5 (color online). Number density (top-left), velocity (top-right), temperature (bottom-left) and dynamic pressure (bottom-right) profiles along the surface streamline.

the number density, slipped velocity, temperature and dynamic pressure change markedly at the vertex, $(X, Y) = (0, \sqrt{3}/2L)$, namely, $h/L = 2$ owing to the strong expansion. The slipped velocity is accelerated around $h/L \sim 2.4$ owing to the vortex generated at the back surface of the triangle prism, in which the profiles of the dynamic pressure approximate to $O(10^{-6})$ because of rarefied effects owing to the expansion.

Figure 6 shows profiles of q^x and $(q^x)_{\mathrm{NSF}}$ along the SSL or WSL (top), profiles of $(q_p^x)_{\mathrm{NSF}}$ and $|(q_p^x)_{\mathrm{NSF}}/(q_t^x)_{\mathrm{NSF}}|$ along the SSL or WSL (middle), and profiles of ϖ and ϖ_{NSF} along the SSL or WSL (bottom). Profiles of q^x can be approximated by q^x_{NSF} along the SSL except for the inside part of the shock wave and the vicinity of the wall owing to the strong nonequilibrium, as shown in the top-left of Fig. 6. On the other hand, profiles of q^x cannot be approximated by q^x_{NSF} along the WSL as shown in the top-right of Fig. 6, because of rarefied effects behind the triangle prism. $(q_p^x)_{\mathrm{NSF}}$ along the SSL increases with the increase in θ_∞ (u^x_∞), as shown in the middle-left of Fig. 6. $(q_p^x)_{\mathrm{NSF}}$ obtained with $\zeta_\infty = 45$, 60 and 75 has a finite value inside the shock structure and thermal boundary layer $1 \leq -X/L \leq 1.3$ on the SSL. Additionally, the sign of $(q_p^x)_{\mathrm{NSF}}$ obtained with $\zeta_\infty = 45$, 60 and 75 is an opposite to that of q^x along the SSL. $(q_p^x)_{\mathrm{NSF}}$ obtained with $\zeta_\infty = 45$, 60 and 75 has a negative peak at the wall $(X, Y) = (0, 0)$ and a positive peak around $X/L \sim 2.4$ on the WSL, as shown in the middle-right of Fig. 6. $|(q_p^x)_{\mathrm{NSF}}/(q_t^x)_{\mathrm{NSF}}|$ obtained with $\zeta_\infty = 45$, 60 and 75 on the SSL are on the order of $\sim 10^{-2}$–10^{-1} inside the shock wave and in the order of $\sim 10^{-3}$–10^{-2} in the thermal boundary layer, as shown in the middle-left of Fig. 6. The order of $|(q_p^x)_{\mathrm{NSF}}/(q_t^x)_{\mathrm{NSF}}|$ obtained with $\zeta_\infty = 45$, 60 and 75 on the WSL changes from 10^{-3} to 10, as shown in the middle-right of Fig. 6. Consequently, $(q_p^x)_{\mathrm{NSF}}$ becomes non-negligible in the thermally relativistic regime, in which $\theta/(nh_E)$ in Eq. (24) is finite. The order of the dynamic pressure (ϖ) obtained with $\zeta_\infty = 45$, 60 and 75 is one digit smaller than that approximated by the relativistic NSF law (ϖ_{NFS}) on the SSL, as shown in the bottom-left of Fig. 6. Additionally, the sign of ϖ is an opposite to that of ϖ_{NFS} in both the shock structure and thermal boundary layer on the SSL. Such remarkable differences between ϖ and ϖ_{NSF} are obtained on the WSL, as shown in the bottom-right of Fig. 6. Such discriminating behavior of the dynamic pressure cannot be described without considering the Burnett order approximation [28]. In particular, the negative ϖ at the vicinity of the wall, $(X, Y) \sim (-L, 0)$, is generated using terms above the Burnett order approximation, because ϖ_{NSF}

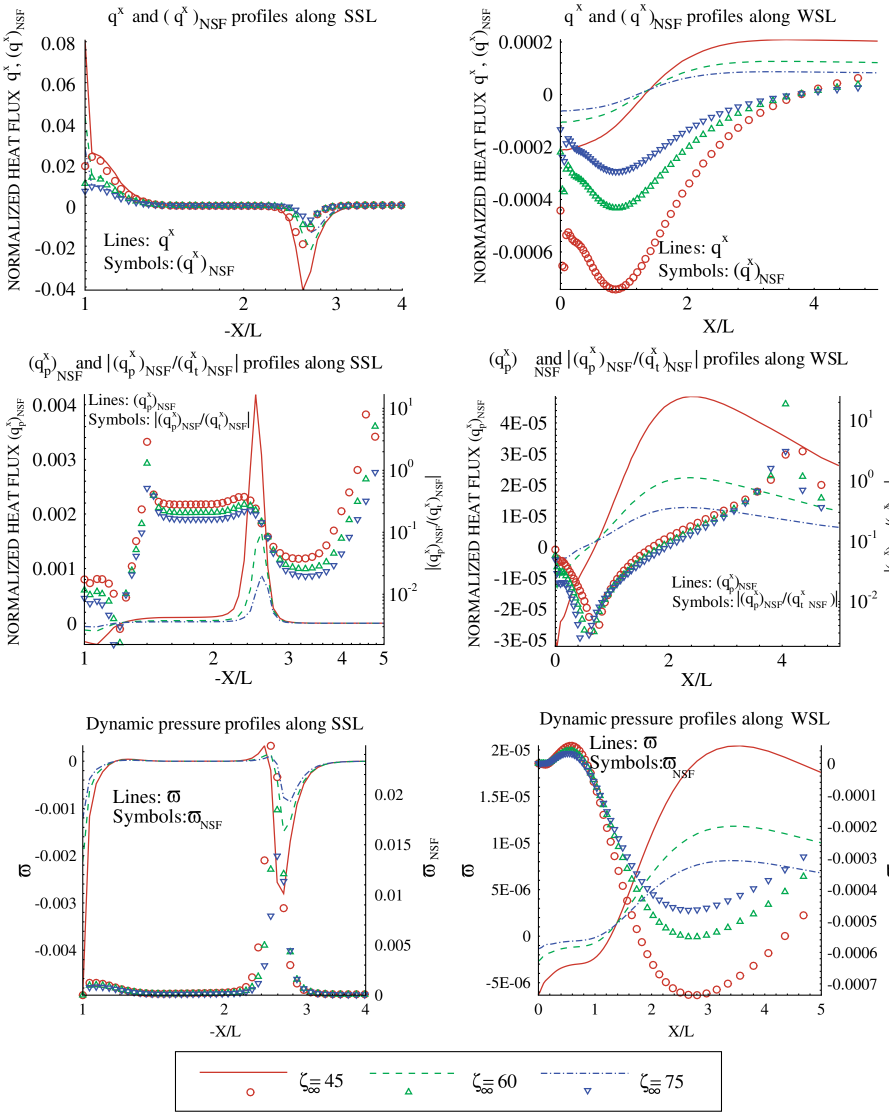

FIG. 6 (color online). q^x and $(q^x)_{\rm NSF}$ profiles along the stagnation streamline (top-left), q^x and $(q^x)_{\rm NSF}$ profiles along the wake streamline (top-right), $(q^x_p)_{\rm NSF}$ and $|q^{xp}_{\rm NSF}/q^{xt}_{\rm NSF}|$ profiles along the stagnation streamline (middle-left), $(q^x_p)_{\rm NSF}$ and $|q^{xp}_{\rm NSF}/q^{xt}_{\rm NSF}|$ profiles along the wake streamline (middle-right), ϖ and $\varpi_{\rm NSF}$ profiles along the stagnation streamline (bottom-left), and ϖ and $\varpi_{\rm NSF}$ profiles along the wake streamline (bottom-right).

approximates to zero at $(X, Y) \sim (-L, 0)$, as shown in the bottom-left of Fig. 6.

We explicitly expressed the relativistic effects on the relativistic NSF equation in Sec. III. Here, effects derived from $\mathcal{S}_0$ and $\mathcal{S}_1$ defined in Eq. (34) are considered to estimate the relativistic effects on the convection of fluids. In the relativistic NSF equation, the time-derivative terms are set to zero, because the flow field is under the steady state. At first, we compare $\rho\mathcal{S}_0 = \rho u^x \partial \ln\gamma/\partial x$ with $\partial \rho u^x/\partial x$ in Eq. (31) on the SSL. The top-left of Fig. 7 shows $\rho u^x \partial \ln\gamma/\partial x$ and $\partial \rho u^x/\partial x$ along the SSL. $\rho u^x \partial \ln\gamma/\partial x$ obtained with $\zeta_\infty = 45$, 60, and 75 has a negative peak around the middle of the shock wave and approximates to zero in other regions. Consequently, relativistic effects derived from the Lorentz contraction are not negligible inside the shock wave. Next, we compare $\rho (u^x)^2 \mathcal{S}_1 = \rho (u^x)^2 \partial \ln G\gamma^2/\partial x$ with $\partial \rho (u^x)^2/\partial x$ in Eq. (32). The top-right of Fig. 7 shows profiles of $\rho (u^x)^2 \partial \ln G\gamma^2/\partial x$ and $\partial \rho (u^x)^2/\partial x$ along the SSL. $\rho (u^x)^2 \partial \ln G\gamma^2/\partial x$ obtained with $\zeta_\infty = 45$, 65 and 75 has a peak around the middle of the shock wave. However, $|\frac{\rho (u^x)^2 \partial \ln G\gamma^2/\partial x}{\partial \rho (u^x)^2/\partial x}|$ is smaller than $|\frac{\rho u^x \partial \ln\gamma/\partial x}{\partial \rho u^x/\partial x}|$. To comprehend the thermally relativistic effects via G in $\rho (u^x)^2 \partial \ln G\gamma^2/\partial x$ and effects via the Lorentz factor γ separately, two limits are considered. One is $\lim_{\gamma\to 1} \rho (u^x)^2 \partial \ln G\gamma^2/\partial x = \rho (u^x)^2 \partial \ln G/\partial x$, which reveals only thermally relativistic effects. The other is the thermally nonrelativistic limit $(\zeta \to \infty)$, $\lim_{G\to 1} \rho (u^x)^2 \partial \ln G\gamma^2/\partial x = \rho (u^x)^2 \partial \ln\gamma^2/\partial x$. The bottom-left of Fig. 7 shows profiles of

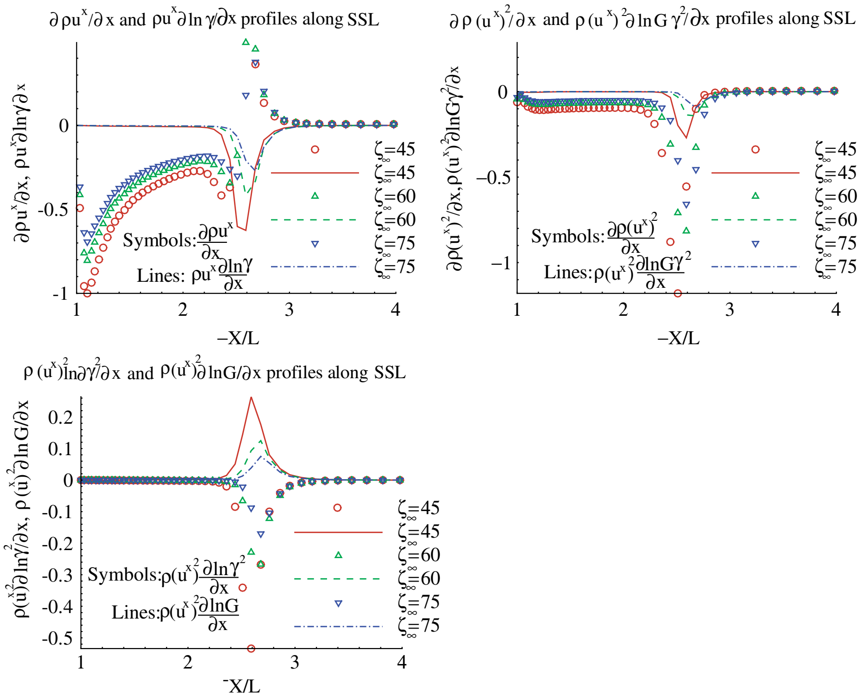

FIG. 7 (color online). $\frac{\partial \rho u^x}{\partial x}$ and $\rho \mathcal{S}_0 (= \rho u^x \frac{\partial \ln \gamma}{\partial x})$ profiles along the stagnation streamline (top-left), $\frac{\partial \rho (u^x)^2}{\partial x}$ and $\rho (u^x)^2 \mathcal{S}_1 (= \rho (u^x)^2 \times \frac{\partial \ln G \gamma^2}{\partial x})$ profiles along the stagnation streamline (top-right), and $\rho (u^x)^2 \partial \ln G / \partial x$ and $\rho (u^x)^2 \partial \ln \gamma^2 / \partial x$ profiles along the stagnation streamline (bottom-left).

$\rho (u^x)^2 \partial \ln G / \partial x$ and $\rho (u^x)^2 \partial \ln \gamma^2 / \partial x$ for $\zeta_\infty = 45$, 60 and 75 along the SSL. As shown in the bottom-left of Fig. 7, the sign of $\rho (u^x)^2 \partial \ln G / \partial x$ is opposite to that of $\rho (u^x)^2 \partial \ln \gamma^2 / \partial x$ whereas $\rho (u^x)^2 \partial \ln G / \partial x$ is of the same order as $\rho (u^x)^2 \partial \ln \gamma^2 / \partial x$. Consequently, thermally relativistic effects via $\rho (u^x)^2 \partial \ln G / \partial x$ and effects by the Lorentz factor γ via $\rho (u^x)^2 \partial \ln \gamma^2 / \partial x$ cancel each other out. Therefore, $|\frac{\rho (u^x)^2 \partial \ln G \gamma^2 / \partial x}{\partial \rho (u^x)^2 / \partial x}|$ becomes smaller than $|\frac{\rho u^x \partial \ln \gamma / \partial x}{\partial \rho u^x / \partial x}|$. However, relativistic effects via the $\rho (u^x)^2 \partial \ln G \gamma^2 / \partial x$ are non-negligible in comparison with $\partial \rho (u^x)^2 / \partial x$ on the SSL, as shown in the top-left of Fig. 7.

Figure 8 shows obtained distribution functions f and equilibrium distribution functions $f^{(0)}$ at $(X, Y) = (-L, 0)$ (A), $(X, Y) = (-1.53L, 0)$ (B), $(X, Y) = (-2.59L, 0)$ (C), $(X, Y) = (-3.28L, 0)$ (D) along the SSL and at $(X, Y) = (0, 0)$ (E), $(X, Y) = (0.47L, 0)$ (F), $(X, Y) = (1.21L, 0)$ (G), $(X, Y) = (3.56L, 0)$ (H) along the WSL obtained using the AW model with $\zeta_\infty = 45$, 60 and 75, where the location of points (A)–(H) is shown in Fig. 1. As shown in Fig. 8(a), distribution functions obtained using the AW model with $\zeta_\infty = 45$, 60 and 75 indicate strong nonequilibrium state on the stagnation point (A), in which distributions are discontinuous at $v^x/c = 0$ owing to the diffusive reflection from the wall for $v^x/c < 0$. At point (B), distribution functions obtained by the AW model with $\zeta_\infty = 45$, 60 and 75 approximate to the equilibrium state as shown in Fig. 8(b). At point (C), which corresponds to interior of the shock wave, distribution functions obtained by the AW model with $\zeta_\infty = 45$, 60 indicate a strong nonequilibrium state, whereas the distribution function obtained using the AW model with $\zeta_\infty = 75$ is weakly nonequilibrium state, as shown in Fig. 8(c). At point (D), which corresponds to the emergence regime of the shock wave, distribution functions f obtained using the AW model with $\zeta_\infty = 45$, 60 and 75 have overpopulations at the negative velocity tail in comparison with equilibrium distribution functions $f^{(0)}$. At point (E), distribution functions obtained using the AW model with $\zeta_\infty = 45$, 60 and 75 indicate a strong nonequilibrium state, in which distribution functions are discontinuous at $v^x/c = 0$ owing to diffusive reflections from the wall for $0 < v^x/c$, as shown in Fig. 8(e). At points (F) and (G), distribution functions f obtained with $z_\infty = 45$ and 60 are still nonequilibrium, whereas the distribution function f obtained with $\zeta_\infty = 75$ is similar to equilibrium distribution function $f^{(0)}$ as shown in Figs. 8(f) and 8(g). At point (H), distribution functions f obtained with $z_\infty = 45$ and 60 approximate to $f^{(0)}$, as shown in Fig. 8(h).

V. CONCLUDING REMARKS

Supersonic flow of thermally relativistic matter around the triangle prism is numerically analyzed using the AW model. The uniform flow is sufficiently rarefied to observe the shock wave structure, whose profile is not approximated using the relativistic NSF equation. From obtained numerical results, the number density and temperature behind shock increase following the relativistic

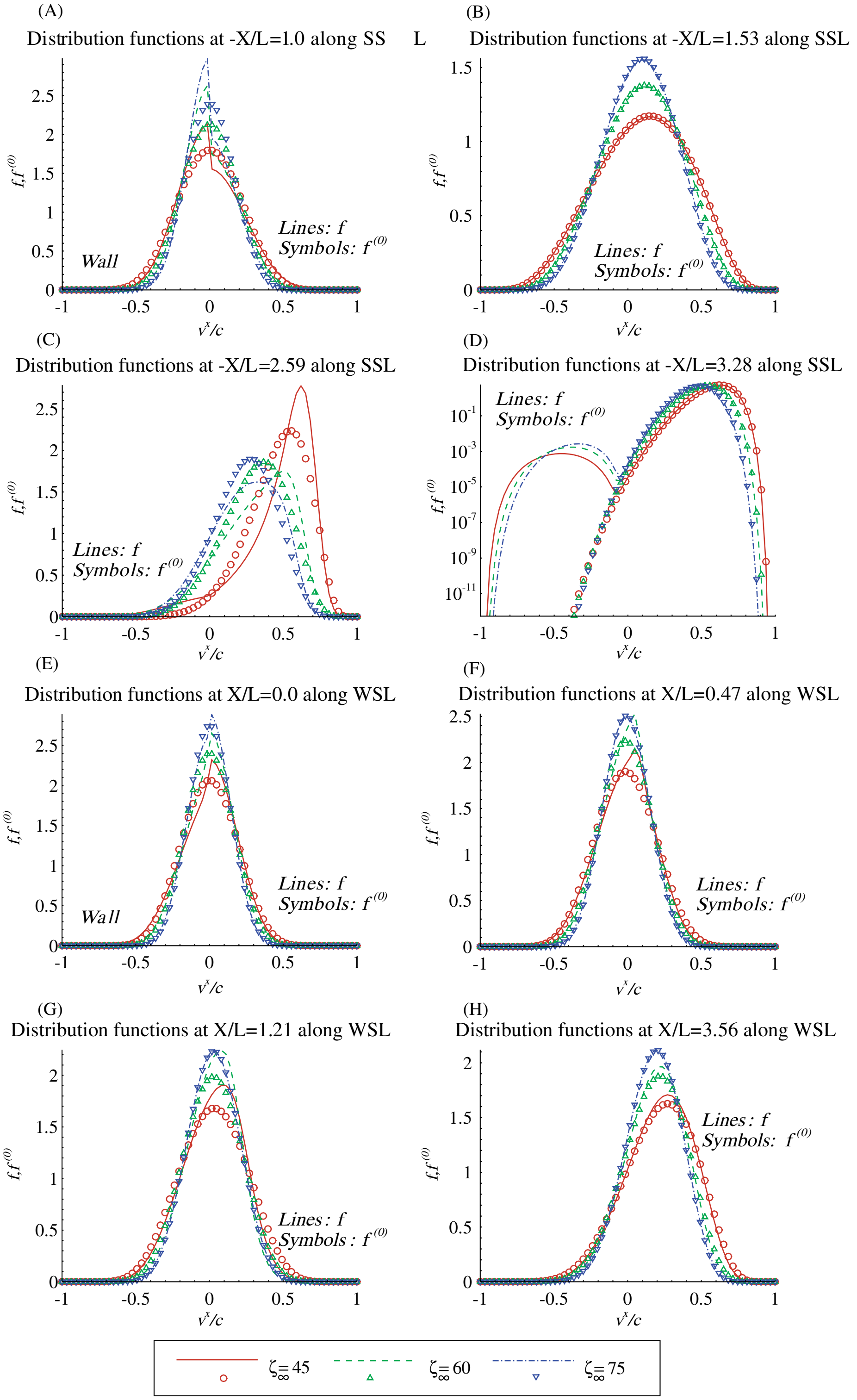

FIG. 8 (color online). Distribution functions at $-X/L = 1.0$ (A), $-X/L = 1.53$ (B), $-X/L = 2.59$ (C), $-X/L = 3.28$ (D) along the SSL and at $X/L = 0.0$ (E), $X/L = 0.47$ (F), $X/L = 1.21$ (G), $X/L = 3.56$ (H) along the WSL.

Rankine-Hugoniot relation, when the temperature and velocity of the uniform flow increase under the condition of the same Mach number. Such relativistic effects are considered from two aspects. One is effect derived from the Lorentz contraction. The other is the thermally relativistic effect. The change in convections of the mass and momentum owing to such two types of relativistic effects is numerically confirmed. In particular, the change in convections owing to relativistic effects is remarkable inside the shock wave. The x-component heat flux along the SSL can be roughly approximated by the relativistic NSF law except for the vicinity of the wall and middle of the shock wave. On the other hand, the x-component heat flux along the WSL cannot be approximated by the relativistic NSF law owing to the rarefied effects. Additionally, the heat flux via the gradient of the static pressure is non-negligible owing to the thermally relativistic effects. The profile of the dynamic pressure is different from that approximated by the relativistic NSF law in the flow field. The description of the dynamic pressure requires further considerations including the Burnett order approximation.

[1] W. A. Hiscock and J. B. Lail, Phys. Rev. D **37**, 869 (1988).
[2] D. H. Rischke, H. Stöcker, and W. Greiner, Phys. Rev. D **42**, 2283 (1990).
[3] J. M. Marti, J. M. Ibàñez, and J. A. Miralles, Phys. Rev. D **43**, 3794 (1991).
[4] W. A. Hiscock and L. Lindblom, Phys. Rev. D **31**, 725 (1985).
[5] C. Eckart, Phys. Rev. **58**, 919 (1940).
[6] L. D. Landau and E. M. Lifshitz, *Fluid Mechanics* (Pergamon Press., Oxford, 1987), 2nd. ed..
[7] K. Tsumura and T. Kunihiro, Phys. Lett. B **668**, 425 (2008).
[8] J. M. Stewart, *Non-Equilibrium Relativistic Kinetic Theory*, Lecture notes in Phys. Vol. 10 (Springer, Heidelberg, 1971).
[9] R. Geroch and L. Lindblom, Phys. Rev. D **41**, 1855 (1990).
[10] J. Peralta-Ramos and E. Calzetta, Phys. Rev. C **82**, 054905 (2010).
[11] T. Koide, G. S. Denicol, Ph. Mota, and T. Kodama, Phys. Rev. C **75**, 034909 (2007).
[12] P. Kostädt and M. Liu, Phys. Rev. D **62**, 023003 (2000).
[13] P. Van and T. S. Biro, Eur. Phys. J. Special Topics **155**, 201 (2008).
[14] I. Bouras, E. Molnár, H. Niemi, Z. Xu, A. El, O. Fochler, F. Lauciello, C. Greiner, and D. H. Rischke, J. Phys. Conf. Ser. **230**, 012045 (2010).
[15] D. Duez, Y. T. Liu, S. L. Shapiro, and B. C. Stephens, Phys. Rev. D **69**, 104030 (2004).
[16] M. Dudynski and M. L. Ekiel-Jezewska, Phys. Rev. Lett. **55**, 2831 (1985).
[17] F. Peano, M. Marti, L. O. Silva, and G. Coppa, Phys. Rev. E **79**, 025701(R) (2009).
[18] I. Bouras, E. Molnár, H. Niemi, Z. Xu, A. El, O. Fochler, C. Greiner, and D. H. Rischke, Phys. Rev. C **82**, 024910 (2010).
[19] P. L. Bhatnagar, E. P. Gross, and M. Krook, Phys. Rev. **94**, 511 (1954).
[20] C. Marle, C.R. Hebd. Seances Acad. Sci. **260**, 6539 (1965).
[21] J. L. Anderson and H. R. Witting, Physica (Amsterdam) **74**, 466 (1974).
[22] M. Mendoza, B. M. Boghosian, H. J. Herrmann, and S. Succi, Phys. Rev. D **82**, 105008 (2010).
[23] T. K. Nakamura, Europhys. Lett. **88**, 40009 (2009).
[24] D. Cubero, J. Casado-Pascual, J. Dunkel, P. Talkner, and P. Hanggi, Phys. Rev. Lett. **99**, 170601 (2007).
[25] R. Yano, K. Suzuki, and H. Kuroda, Phys. Rev. D **80**, 123506 (2009).
[26] C. Cercignani and G. Kremer, *The Relativistic Boltzmann Equation: Theory and Applications*, Progress in Math. Phys. Vol. 22 (Springer-Verlag, Berlin, 2002).
[27] C. Cercignani, *The Boltzmann Equation and Its Applications*, Lecture Series in Mathematics Vol. 68 (Springer-Verlag, Berlin, 1988).
[28] L. L. Samojeden and G. M. Kremer, Physica A (Amsterdam) **307**, 354 (2002).
[29] R. Yano, K. Suzuki, and H. Kuroda, Physica A (Amsterdam) **381**, 8 (2007).
[30] H. C. Yee, *A Class of High-Resolution Explicit and Implicit Shock-Capturing Methods*, Lecture Series Vol. 4 (von Karman Institute for Fluid Dynamics, Rhode-St-Genese, Belgium, 1989).
[31] In Eckart's first-order hydrodynamics [5], the relativistic NSF law of the heat flux is written in the form, $q^\alpha = \lambda(\nabla^\alpha T - \frac{T}{c^2} DU^\alpha)$ $(D \equiv U^\alpha \partial_\alpha)$. This definition of q^α can be reduced to Eq. (24) using a momentum-balance equation under the equilibrium condition, namely, $\frac{nh_E}{c^2} DU^\alpha = \nabla^\alpha p$. The relativistic NSF law, which is introduced by the Chapmann-Enskog expansion, follows Eq. (24) as discussed in [26].
[32] J. R. Wilson and G. J. Mathews, *Relativistic Numerical Hydrodynamics* (Cambridge University Press, Cambridge, UK, 2003).
[33] In the limit of $\zeta \longrightarrow 0$, the bulk viscosity approximates to $\eta_{\mathrm{A.W.}} \sim O(\zeta^3)$ [21], the heat conductivity approximates to $\lambda_{\mathrm{A.W.}} \sim O(1)$ [21] and the viscosity coefficient approximates to $\mu_{\mathrm{A.W.}} \sim O(\zeta^{-1})$ [21]. As a result, the dynamic pressure divided by $\lim_{\zeta \rightarrow 0} G = O(\zeta^{-1})$ approximates to $\eta_{\mathrm{A.W.}}/G \sim O(\zeta^4)$, and the pressure deviator divided by G approximates to $\mu_{\mathrm{A.W.}}/G \sim O(1)$, namely, a constant value. As a result, dissipative terms $\frac{\Pi^i}{G\gamma^2}$ and Λ in Eqs. (32) and (33), approximate to nondivergent values under $\zeta \longrightarrow 0$.
[34] A. M. Taub, Phys. Rev. **74**, 328 (1948).
[35] The flow slip on the wall surface is non-negligible owing to the rarefied effect [27].